Accepted Article

Title: Dicarboxylic Acid-Assisted Surface Oxide Removal and Passivation of Indium Antimonide Colloidal Quantum Dots for Short-Wave Infrared Photodetectors

Authors: Yangning Zhang, Pan Xia, Benjamin Rehl, Darshan H. Parmar, Dongsun Choi, Muhammad Imran, Yiqing Chen, Yanjiang Liu, Maral Vafaie, Chongwen Li, Ozan Atan, Joao M. Pina, Watcharaphol Paritmongkol, Larissa Levina, Oleksandr Voznyy, Sjoerd Hoogland, and Edward Hartley Sargent

This manuscript has been accepted after peer review and appears as an Accepted Article online prior to editing, proofing, and formal publication of the final Version of Record (VoR). The VoR will be published online in Early View as soon as possible and may be different to this Accepted Article as a result of editing. Readers should obtain the VoR from the journal website shown below when it is published to ensure accuracy of information. The authors are responsible for the content of this Accepted Article.

WILEY VCH

RESEARCH ARTICLE

Dicarboxylic Acid-Assisted Surface Oxide Removal and Passivation of Indium Antimonide Colloidal Quantum Dots for Short-Wave Infrared Photodetectors

Yangning Zhang,[a] Pan Xia,[a] Benjamin Rehl,[a] Darshan H. Parmar,[a] Dongsun Choi,[a] Muhammad Imran,[a] Yiqing Chen,[a] Yanjiang Liu,[a] Maral Vafaie,[a] Chongwen Li,[a] Ozan Atan,[a] Joao M. Pina,[a] Watcharaphol Paritmongkol,[a,b] Larissa Levina,[a] Oleksandr Voznyy,[c] Sjoerd Hoogland,[a] Edward H. Sargent*[a]

---

[a]   Dr. Y. Zhang, Dr. P. Xia, Dr. B. Rehl, D. H. Parmar, Dr. D. Choi, Dr. M. Imran, Dr. Y. Chen, Y. Liu, Dr. M. Vafaie, Dr. C. Li, O. Atan, Dr. J. M. Pina, Dr. W. Paritmongkol, Dr. L. Levina, Dr. S. Hoogland, and Prof. Dr. E. H. Sargent

        Department of Electrical and Computer Engineering

        University of Toronto

        10 King's College Road, Toronto, Ontario, M5S 3G4, Canada

        E-mail: ted.sargent@utoronto.ca

[b]   Dr. W. Paritmongkol

        Department of Materials Science and Engineering, School of Molecular Science and Engineering

        Vidyasirimedhi Institute of Science and Technology

        Rayong 21210, Thailand

[c]   Prof. Dr. O. Voznyy

        Department of Physical and Environmental Sciences

        University of Toronto (Scarborough)

        1065 Military Trail, Toronto, Ontario, M1C 1A4, Canada

        Supporting information for this article is given via a link at the end of the document.

Abstract: Heavy-metal-free III-V colloidal quantum dots (CQDs) are promising materials for solution-processed short-wave infrared (SWIR) photodetectors. Recent progress in the synthesis of indium antimonide (InSb) CQDs with sizes smaller than the Bohr exciton radius enables quantum-size effect tuning of the bandgap. However, it has been challenging to achieve uniform InSb CQDs with bandgaps below 0.9 eV, as well as to control the surface chemistry of these large-diameter CQDs. This has, to date, limited the development of InSb CQD photodetectors that are sensitive to ≥1400 nm light. Here we adopt solvent engineering to facilitate a diffusion-limited growth regime, leading to uniform CQDs with a bandgap of 0.89 eV. We then develop a CQD surface reconstruction strategy that employs a dicarboxylic acid to selectively remove the native In/Sb oxides, and enables a carboxylate-halide co-passivation with the subsequent halide ligand exchange. We find that this strategy reduces trap density by half compared to controls, and enables electronic coupling among CQDs. Photodetectors made using the tailored CQDs achieve an external quantum efficiency of 25% at 1400 nm, the highest among III-V CQD photodetectors in this spectral region.

Introduction

Short-wave infrared (SWIR, ranging from 1000 to 2500 nm) photodetectors serve medical imaging, telecommunications, autonomous vehicles, and consumer electronics.[1,2] SWIR operation at the wavelength of 1400 nm, in particular, offers eye safety, the availability of low-cost optical sources, and low background interference from sunlight.[3]

Colloidal quantum dots (CQDs) are attractive materials for solution-processed photodetectors owing to their size-tunable bandgaps, cost-effectiveness, and compatibility with silicon read-out circuits.[4,5] Present-day CQD SWIR photodetectors typically employ PbS or HgTe CQDs as the active layer,[6–9] which contain RoHS-regulated elements. Recent advances in the synthetic development of III-V CQDs provide access to heavy-metal-free CQD SWIR photodetectors. Indium antimonide (InSb), in particular, with a bulk bandgap of 0.17 eV and a Bohr exciton radius of ~60 nm,[10,11] enables quantum-size effect tuning of the CQD bandgaps over a wide 0.6-1.3 eV range.

To achieve high-performance CQD photodetectors sensitive to 1400 nm light, one must first synthesize uniformly large-diameter CQDs with a bandgap of 0.89 eV. Due to the covalent nature of InSb CQDs, their synthesis relies on highly-reactive precursors, strong reducing agents, and high reaction temperatures.[12–16] The nucleation and growth of large-diameter CQDs is not well-controlled under these conditions, leading to size distributions of more than 10%. Non-uniform CQDs suffer from an inhomogeneous energy landscape detrimental to device performance.[17,18]

In addition, the surface chemistry and the electronic structure of large-diameter InSb CQDs are not thoroughly understood. The oxophilic nature of In and Sb makes InSb CQDs prone to surface oxidation, especially during high temperature synthesis.[15] Insulating metal oxides formed as a result of oxidation produce a barrier to charge transport and may introduce surface trap states.

RESEARCH ARTICLE

Improving charge transport and minimizing surface defects is crucial for the successful integration of these CQDs into optoelectronic devices.

Due to the challenges in synthetic control and surface management, the performance of InSb CQD SWIR photodetectors has lagged behind those of other III-V CQDs.[15,19,20] So far, photodetectors that employ InSb CQDs as the active layer have exhibited a specific detectivity of 1.5×10^6 Jones at 1400 nm, three orders of magnitude lower than that of In(As,P) CQD photodetectors in this spectral region.[21,22]

Here we develop a synthesis of InSb CQDs that leads to a size distribution narrower than 10% and a first excitonic peak at 1400 nm by control over CQD nucleation and growth kinetics aided by solvent engineering. We use a combination of non-coordinating and coordinating solvents to produce size focusing of CQDs within a diffusion-limited growth regime. From density functional theory (DFT) calculations, we find that oxidation of the (111) facets creates trap states inside the bandgap. To address this challenge, we design a selective etching strategy using a dicarboxylic acid as the etchant, which simultaneously removes the native oxides and oleic acid ligands and coordinates with surface atoms. A subsequent halide exchange step is needed to achieve complete surface passivation and to enhance the electronic coupling between CQDs. Compared to the acid-etched or one-step halide-exchanged CQDs, the cascade-modified CQDs exhibit a reduced trap state density and an increased charge carrier mobility. Using the synthetic and materials processing approach, we report SWIR photodetectors with a low dark current of 9.6×10^{-3} mA cm^{-2} and an external quantum efficiency (EQE) of 25%. The detectivity of 1.4×10^{11} Jones at 1400 nm achieved in our photodetectors shows a 140x improvement compared to prior reports of III-V CQD photodetectors.[21]

Results and Discussion

Uniform InSb quantum dots were synthesized using a modified heat-up method (see Supporting Information for experimental procedures).[15] The injection of super hydride into the precursor mixture of InCl$_3$ and SbCl$_3$ dissolved in oleylamine (OLAM) triggers the co-reduction of In^{3+} and Sb^{3+}, as the solution immediately changes from clear to black color. At elevated temperatures In^0 and Sb^0 monomers are formed,[13] allowing for the nucleation and growth of InSb CQDs, and annealing at 280-290 °C for 30 min is needed to achieve large diameter CQDs. After cooling, oleic acid was added to the reaction product to enhance the colloidal stability of CQDs in toluene. To tune the concentration of monomers and enable a balanced nucleation and growth rate needed for obtaining large CQDs, we introduced heptadecane to the reaction mixture. Since heptadecane as a 17-carbon high-boiling point alkane does not have any functional group, it does not attach to the surface of CQDs, but acts as a

non-coordinating solvent to dilute the monomer concentration. Furthermore, with its steric hindrance heptadecane also facilitates a diffusion-limited growth regime by hindering the diffusion of monomers to the nuclei, which promotes crystal growth to obtain large CQDs, as illustrated in Scheme 1.

In Figure 1a, by optimizing the volume of heptadecane and the concentration of In^{3+}, we obtained CQDs with a sharp excitonic peak at 1400 nm (bandgap of 0.89 eV, see Figure S1a for the absorption spectra under different In^{3+} concentrations). X-ray diffraction confirmed that the as-synthesized CQDs exhibited the zinc blende InSb crystal structure (Figure S2).[23a] The CQDs showed an average size of 4.9 nm with a size distribution in the range of 8-10%, as shown in the high-angle annular dark field scanning transmission electron microscopy (HAADF-STEM) image in Figure 1b (size histogram is provided in Figure S2). These results suggested that the presence of heptadecane promotes the growth of large CQDs. In contrast, we found that replacing the non-coordinating heptadecane completely with the coordinating solvent OLAM resulted in blue-shifted absorption peaks centered in the range of 1230-1330 nm (Figure S1b), suggesting that CQDs with smaller diameters were obtained. We hypothesize that the attachment of excess OLAM favors the growth of smaller CQDs.

We examined the optical properties of large CQDs with a bandgap of 0.89 eV in more detail. Based on the calculated size-dependent quantum state levels of InSb CQDs, the first excitonic peak at 1400 nm (0.89 eV) in Figure 1a was believed to originate from 1S$_{3/2}$(h) − 1S(e) transition.[13,23b] The broad absorption feature at 1000-1100 nm (1.13-1.24 eV) is likely the second excitonic peak, and further investigation is needed to understand the corresponding electronic transitions. We observed room-temperature photoluminescence (PL) centered at 1507 nm for these CQDs with a Stokes shift of 117 nm. Using PbS CQDs as a reference, we estimated that the PL quantum yield (QY) of InSb CQDs is 2-3% (Figure S3). The time-resolved PL (TRPL) is fitted with a three-exponential decay model, with the fast decay components of 3.2 ns and 16.3 ns, and a slow decay component of 66.6 ns (Figure S4 and Table S1). The slow component presumably corresponds to the radiative lifetime, and is similar to that of previously-reported 3.7 nm InSb CQDs (71 ns at 300 K).[16] The fast components could arise from non-radiative processes.

We performed transient absorption (TA) measurements for as-synthesized 4.9 nm InSb CQDs (Figure S5 and Table S2). The TA spectral kinetic trace is fitted with a single-exponential decay with a lifetime of 1.5 ns, which is 50x longer than the 31 ps TA lifetime reported for 4.0 nm InSb CQDs.[24a] This suggests slower exciton trapping in our InSb CQDs compared to prior syntheses. In comparison with PbS CQDs,[24b] however, the TA lifetime of InSb CQDs appears to be shorter due to two possible reasons. First, covalent III-V CQDs have more bulk defects (such as lattice disorder)[24c] than ionic Pb chalcogenides, which could cause faster exciton trapping. In addition, the shorter TA lifetime is also related to surface defects such as oxidation and dangling bonds.[24d]
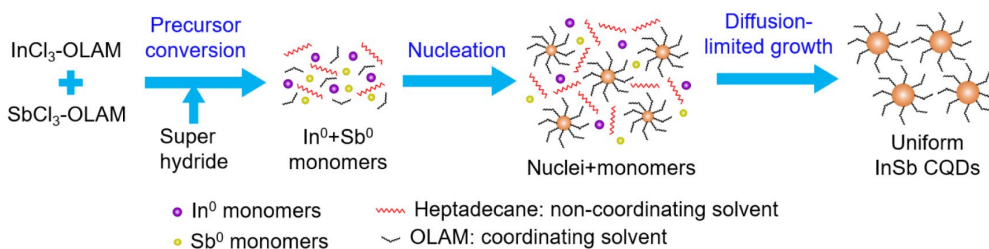
Scheme 1. Illustration of InSb CQD synthesis process. Three stages are involved: precursor conversion, nucleation, and diffusion-limited growth. The solvent combination of heptadecane and oleylamine enables the uniform growth of InSb CQDs.
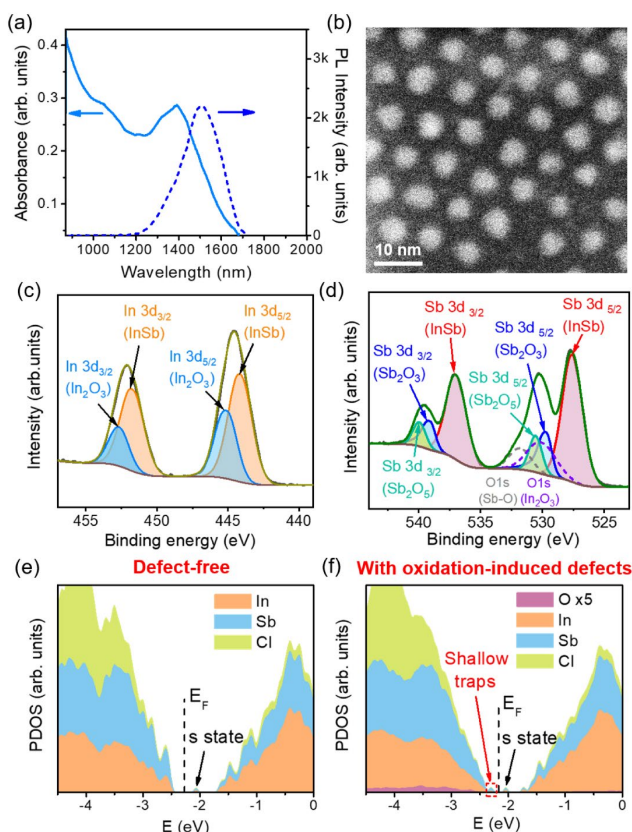
Figure 1. Materials characterization of as-synthesized InSb CQDs and DFT simulation. (a) Absorption and PL spectra, and (b) HAADF-STEM image of as-synthesized InSb CQDs. XPS analysis of CQDs: (c) In 3d spectra; (d) Sb 3d and O 1s spectra. Deconvolution of In 3d peaks shows a coexistence of InSb and In_2O_3, and the Sb 3d peaks show a coexistence of InSb, Sb_2O_3, and Sb_2O_5. DFT projected density of states (PDOS) for (e) a charge-balanced CQD showing a clean bandgap, and (f) a CQD with oxygen-induced structure distortions that create shallow trap states. The traps are not localized on oxygen. E_F represents the Fermi level. The bump at around -2.1 eV is the s state of the conduction band.

Due to the oxophilic nature of In and Sb, bulk InSb oxidizes easily when exposed to air at room temperature, and stable In/Sb oxides quickly form on the surface of InSb.[25,26] The CQDs are more susceptible to oxidation, owing to their large surface-to-volume ratio. We observed the presence of In_2O_3 and Sb_2O_x (x=3 or 5) in as-synthesized CQDs, as determined from X-ray

photoelectron spectroscopy (XPS) analysis (Figures 1c and 1d). Since the synthesis and purification processes were air-free and water-free, we posited that the native oxides were likely formed *in-situ* during the high-temperature annealing process at 280-290 °C, where the oxygen could be released from the oxygen-containing functional groups of the solvents or ligands and consequently chemisorbed on the CQD surface.

We carried out DFT calculations to understand the interaction of oxygen with InSb CQDs and its impact on the surface electronic states. Following the geometries of an InAs CQD model,[27a] we first created a charge-balanced, defect-free InSb CQD, which exhibited a clean bandgap (Figures 1e). Oxygen atoms were introduced to different facets and sites of the CQD (see Figure S6 for details). The oxygen atoms that were initially adsorbed on top of In atoms on the (111) facets penetrated to the subsurface and formed bonding with nearby In and Sb atoms, consistent with the presence of In_2O_3 and Sb_2O_x determined from XPS. We posited that the oxygen penetration is related to the fact that InSb has the largest lattice constant (a=6.48 Å) among the III-V semiconductors. The oxygen itself did not cause any mid-gap states, primarily due to the small bandgap of InSb, so that the oxygen orbitals overlapped and coupled well to the bulk InSb states. However, these metal-oxygen bonds distorted the local structures, resulting in semi-localized shallow trap states near the valence band edge (Figures 1f). These defects potentially lead to p-type behavior in as-synthesized InSb CQDs, similar to that of oxidized PbS CQDs.[27b] Whereas, the oxygen atoms on the (100) facets did not lead to structural distortion or trap state formation. In addition to the oxidation-induced shallow trap states, In_2O_3 and Sb_2O_x formed on the CQDs are insulating, therefore creating a barrier for charge transport.

To enable efficient charge transport between CQDs, we sought to remove the native oxides as well as oxidation-related surface trap states. Oleic acid (OA) is considered the primary capping ligand for InSb CQDs.[15] The insulating OA ligands should be replaced with shorter ligands that minimize the interparticle spacing and completely passivate the surface sites of CQDs. Taking these factors into consideration, we designed a cascade ligand exchange strategy to resurface the CQDs, as illustrated in Figure 2a. The cascade exchange began with an acid etching step to get rid of In and Sb oxides from the CQD surface. In bulk InSb, inorganic acids such as HF or HCl are typically employed for the native oxide removal, but their lack of selectivity can lead to etching of the InSb, surface roughening, or even

RESEARCH ARTICLE

elemental Sb formation.[28,29] This motivated us to explore mild carboxylic acids instead of inorganic acids for resurfacing InSb CQDs. Malonic acid (MA) as a short-chain dicarboxylic acid ligand with moderate acidity (pKa=2.83) was chosen as the etchant, and it offered three-fold functionalities: (1) It selectively removes the native In and Sb oxides through the formation of In and Sb malonate complexes that are washed away easily by solvents, while maintaining the integrity of InSb CQDs. (2) The two carboxyl groups of MA can coordinate with metal atoms in a bidentate bridging mode, which passivates multiple active sites and limits further oxidation.[30] (3) Short-chain MA ligands decrease inter-CQD spacing, thus enhancing the electronic coupling among the CQDs.

The CQD size and crystal structure remained intact after the MA etching step, as confirmed by the high-resolution transmission electron microscopy (HRTEM) in Figure 2b. The lattice spacings

(3.7 Å) of individual CQDs matched with the (111) planes of the zinc blende InSb. MA-treated CQDs showed a significant reduction in the inter-CQD spacing compared to as-synthesized CQDs, as expected for the replacement of long-chain OA ligands with short-chain MA ligands. The Fourier transform infrared (FTIR) spectroscopy analysis (Figure 2c) showed the COO^- stretches that are characteristic of bound OA ligands in as-synthesized CQDs. The peak intensities of CH_2 and CH_3 stretches have decreased significantly in the MA-treated CQDs compared to those of as-synthesized ones, suggesting removal of native OA ligands. In Figures 2c and 2d, the In 3d and Sb 3d XPS spectra showed evidence for the removal of In_2O_3 and Sb_2O_x in the MA-treated InSb CQDs, as the $3d_{3/2}$ and $3d_{5/2}$ peaks of In_2O_3 and Sb_2O_x were greatly reduced. Similar to as-synthesized CQDs, the MA-etched CQDs preserved an In-rich stoichiometry, with an In to Sb ratio of 1.4-1.5 (see Table S3 for XPS elemental analysis).
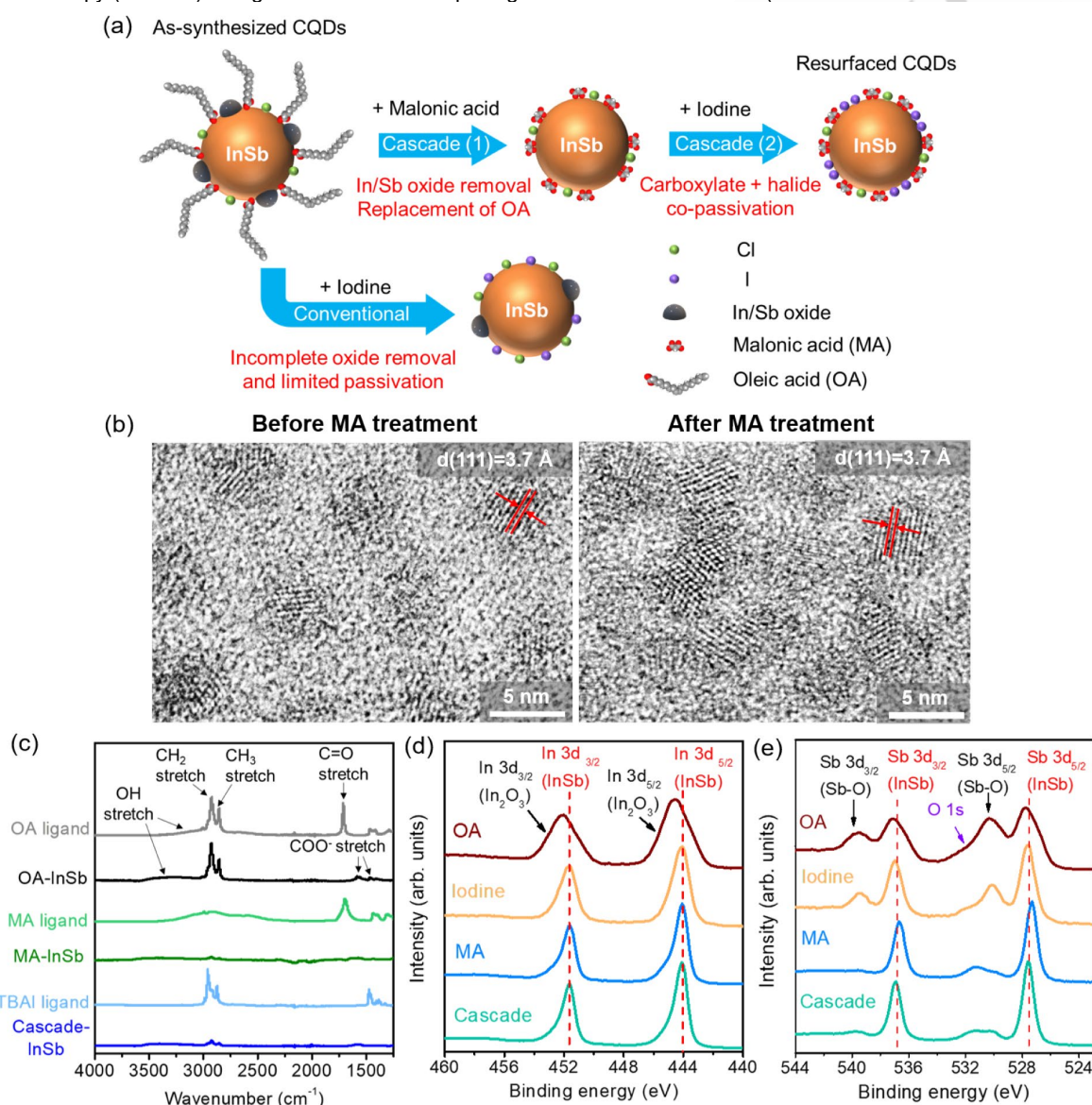
Figure 2. Surface reconstruction strategies for InSb CQDs. (a) Schematic of cascade ligand exchange in comparison with one-step halide exchange. The cascade exchange introduces an etching step prior to the halide exchange step. (b) HRTEM images of CQDs before and after MA treatment. The lattice spacings of 3.7 Å correspond to the (111) planes of the zinc blende InSb. (c) FTIR spectra of pure ligands (OA, MA, and TBAI), OA-capped CQDs, MA-treated CQDs, and cascade-exchanged CQDs. XPS spectra of CQDs before and after different surface modifications: (d) In 3d spectra; (e) Sb 3d spectra.

RESEARCH ARTICLE

To further improve the conductivity of CQDs and achieve complete passivation of surface defects, we introduced iodine ligands following the MA etching step, using tetrabutylammonium iodide (TBAI) as the agent. TBAI was previously reported to create conductive n-type PbS CQDs and enabled high-performance optoelectronic devices.[3,31a] After the complete cascade exchange, the carboxyl group from MA ligands and the iodine from TBAI ligands were present in the CQDs (see Figure S7 for the C 1s and I 3d XPS spectra). In addition, we also noticed the presence of chlorine in the cascade-exchanged CQDs, which presumably originated from $InCl_3$ and $SbCl_3$ precursors used in the synthesis (see Figure S7 for the Cl 2p XPS spectrum). These results suggested a co-passivation of In-rich surfaces with halides (Cl and I) and carboxylate, as illustrated in Figure 2a. The band structures calculated by DFT showed that the co-passivated InSb (111) surface exhibited a clean bandgap, while the bare surface or MA-passivated surface showed states inside the bandgap or no bandgap (Figure S8).

The cascade exchange composed of an oxide removal step and a halide exchange step was more beneficial than the conventional one-step halide exchange, because the oxide removal step created a cleaner surface of CQDs and allowed a higher surface coverage with halides in the subsequent exchange step. XPS spectra in Figure 2d showed that the removal of In_2O_3 was achieved in all the exchanges, as evidenced by the narrower In 3d peaks. The Sb_2O_x peaks were negligible in the cascade-exchanged CQDs, while the one-step iodine-exchanged ones had more prominent Sb_2O_x peaks (Figure 2e). From XPS elemental analysis we found that cascade-exchanged CQDs exhibited 25%

higher halide (Cl and I) to In ratio than did one-step iodine-exchanged CQDs (Table S3).

Compared to as-synthesized CQDs, the cascade-exchanged CQDs were more closely packed, as the average CQD center-to-center distance decreased from 9 nm to 6.5 nm (Figure 3a). This confirmed the replacement of long OA ligands with shorter ligands and facilitated the electronic coupling between CQDs. The average edge-to-edge separation between CQDs after cascade-ligand exchange was 1-1.5 nm, which is a reduction of 45-60% compared to previously published results for a one-step halide exchange.[32] The absorption peaks of MA-treated and cascade-exchanged CQD films were slightly red-shifted compared to the OA-CQD film (Figure 3b), also suggesting the enhanced CQD coupling. The absorption peak of one-step iodine-exchanged CQD film did not shift with respect to OA-CQDs. Photoluminescence was preserved in all the CQD films before and after ligand exchange (Figure S9).

To investigate the charge transport properties of CQDs from different surface modifications, we compared the energy levels calculated from the UV photoelectron spectroscopy (UPS) results and the CQD bandgap of 0.89 eV (Figure S10a). The Fermi levels (E_F) of all CQD films were located closer to their conduction band minimums (E_{CBM}) than to the valence band maximums (E_{VBM}), indicating an n-type behavior. Based on charge-orbital balance analysis, the doping behavior of CQDs typically depends on the stoichiometry of the CQDs and the charges of surface species.[31b] The removal of surface oxygen with a -2 charge together with the introduction of ligands with a –1 charge could create n-type characteristics of CQDs, as observed in InAs and PbS CQDs.[19,31a]
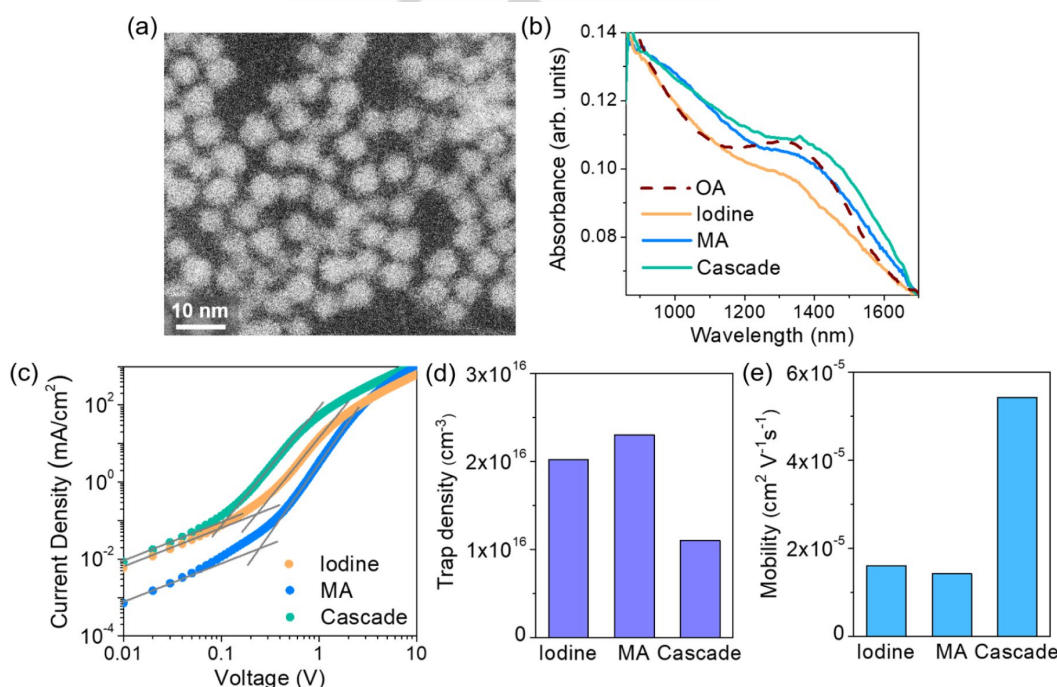

Figure 3. Optical and electronic properties of resurfaced InSb CQDs. (a) HAADF-STEM image of CQDs after cascade ligand exchange. (b) Absorption spectra of OA-capped or various ligand-exchanged CQD films. (c) SCLC curves of CQDs with different surface modifications, and comparison of (d) trap densities and (e) carrier mobilities extracted from SCLC. The grey lines in (c) represent the fits of the ohmic regime and trap-filling regime.

RESEARCH ARTICLE

Space-charge limited current (SCLC) measurements were performed on electron-only devices with the structure of ITO/ZnO/InSb CQDs/LiF/Ag. The SCLC curves of the various ligand-exchanged CQDs demonstrated three regimes: the Ohmic regime, the trap-filling regime, and the SCLC regime (Figure 3c). The trap densities and carrier mobilities were calculated from the trap-filling regime and the SCLC regime, respectively (Figures 3d-3e and Table S4). In comparison with one-step iodine-exchanged or MA-treated CQDs, cascade-exchanged CQDs having substantial oxide removal and effective surface passivation exhibited a reduced trap density of 1.1×10^{16} cm^{-3}. The electron mobility of cascade-exchanged CQDs was 3-4 times higher than that of controls, suggesting better electronic coupling in the former.

Photodetectors with n-i-p structure (Figure 4a) were fabricated using InSb CQDs as the active layer, and ZnO and MoO$_x$ as electron- and hole-transporting layers, respectively. The band diagram is shown in Figure S10b. Cross-section scanning electron microscopy (SEM) analysis (Figure 4b) showed that the CQD layer had a thickness of 140-150 nm. Figure 4c compares the current-voltage (I-V) characteristic metrics for devices made of CQDs from different surface modifications. The cascade-exchanged CQD devices exhibited a rectification ratio (RR,

calculated by dividing the dark current at -1 V by the dark current at 1 V) of 400, which was 13-15x better than that of one-step iodine-exchanged or MA-treated ones. The behavior of dark current can be understood as the summation of several components, including diode current, ohmic current, and trap-assisted leakage current.[33] The improved carrier mobility of the cascade-exchanged CQD devices (as measured by SCLC in Figure 3e) increases ohmic current leading simultaneously to higher forward and reverse dark current. The lower carrier mobility of the controls decreased both forward and reverse dark current by decreasing the ohmic current. In particular, the MA and iodide-exchanged CQDs exhibit 50x and 700x lower forward dark current compared to cascade-exchanged CQDs, suggesting lower ohmic current and consequently lower RR (Figure S11a). Under white light (AM 1.5) illumination, the cascade-exchanged CQD devices showed a short-circuit current (Jsc) of 3.2 mA cm^{-2} (see Figure S12 for the linear scale I-V curve), 1-2 orders of magnitude higher than control devices. This is also a consequence of the higher carrier mobility of cascade-exchanged CQDs than the controls (Figure 3e).
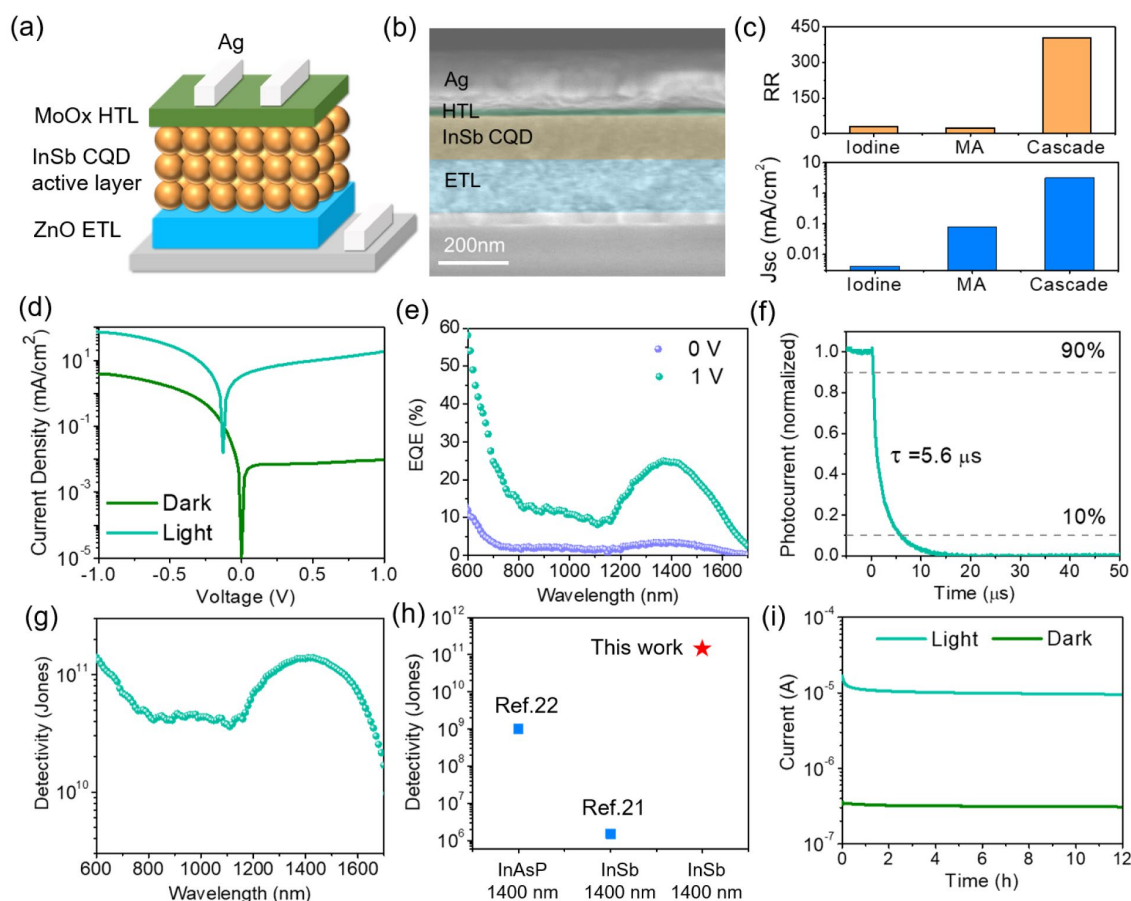
Figure 4. Structure and performance of InSb CQD photodetectors. (a) Schematic and (b) cross-section SEM of the InSb CQD photodetector device stack. (c) Comparison of rectification ratio and short-circuit current of photodetectors that used CQDs from different surface modifications as the active layer. (d) Current density-voltage curves and (e) EQE spectra of cascade-exchanged InSb CQD photodetectors, measured under different reverse bias voltages (0 V and 1 V). (f) Transient photocurrent of InSb CQD photodetectors with a pixel area of 0.2 mm² at 1 V. (g) Specific detectivity as a function of wavelength. (h) Comparison of specific detectivity in this work with prior reports of III-V CQD photodetectors that operate at 1400 nm.[21,22] (i) Device operational stability under 0.1 V reverse bias.

RESEARCH ARTICLE

Figures 4d-4g demonstrate the performance of photodetectors with cascade-exchanged InSb CQDs as the active layer. These devices showed a dark current density of 9.6×10^{-3} mA cm^{-2} and a light current density of 18.8 mA cm^{-2} at 1 V reverse bias under AM 1.5 illumination (Figure 4d). Power-dependent I−V was measured using an excitation wavelength of 1450 nm, showing an increase in light current with increasing input power (Figure S11b). The EQE reached a maximum at 1400 nm (Figure 4e), consistent with the CQD absorption peak at 1400 nm. The peak EQE was dependent on the reverse bias voltage applied, increasing from 3.4% at 0 V to 25% at 1 V. Differences in detailed spectral shape between device EQE and CQD absorption in the range 800-1200 nm can be accounted for via Fabry-Perot interference.[34a] At 1400 nm, the EQE of the InSb CQD photodetectors reported herein shows a 25-fold improvement over the highest EQE previously-reported for InAsP CQD photodetectors,[22] and a 2-fold improvement compared to the highest EQE previously-reported for InSb CQD photodetectors.[34b] We found that employing CQDs with size distributions of more than 10% as the active layer resulted in EQEs below 10% at 1 V (Figure S13). Therefore, we attribute the enhanced performance of our photodetectors to the improved uniformity of CQDs from the synthetic optimization combined with the reduced defects and enhanced electronic coupling of CQDs facilitated by the cascade exchange.

The photodetection speed was determined by measuring the transient photocurrent responses (Figure 4f), showing a fall time (the time interval between 10% and 90% of the maximum photocurrent) of 5.6 µs at 1 V for a pixel area of 0.2 mm^2. We believe that the speed can be further improved by increasing the carrier mobilities of CQDs.[34c] In Figure 4g, the photodetectors reached a maximum specific detectivity of 1.4×10^{11} Jones at 1400 nm, which was calculated based on the measured responsivity and noise (Figure S14). The detectivity of our InSb CQD photodetectors was improved by 5 orders of magnitude compared to previously-reported InSb photodetectors, and 140x higher than that of InAsP photodetectors in the same spectral window (Figure 4h).[21,22]

We studied the operational stability of InSb CQD photodetectors by tracking the light current and dark current under 0.1 V reverse bias (Figure 4i). After an initial burn-in in the first 2 h, the light current slowly decreased by another 10% over the course of 10 h. The dark current retained 96% of the initial value after 12 h of operation. In our previous work, PbS CQD photodetectors exhibited a 2-fold increase in dark current after 16 h of operation, which was attributed to the electric field-induced ionic migration in PbS CQDs.[6] The enhanced dark current stability of InSb CQD photodetectors in this work suggests that the covalent nature of III-V CQDs offers the advantage of stable device operation.

Conclusion

In summary, we report uniform InSb CQDs with an average size of 4.9 nm by facilitating the diffusion-limited growth of CQDs, and they exhibit a distinct absorption peak centered at 1400 nm.

Finding that the surface metal (In/Sb) oxides act as a source of trap states, we design a CQD resurfacing strategy that begins with a dicarboxylic acid to selectively remove the oxides as well as to replace the native ligands. The acid-treated CQDs are then exchanged with halide ligands to achieve carboxylate-halide co-passivation and enhance electronic coupling. We find using space-charge limited transport measurements that the trap state density of resurfaced CQDs is reduced by half compared to single-step halide-exchanged CQDs. The resulting photodetectors achieve an EQE of 25%, outperforming prior reports of III-V CQD photodetectors operating at 1400 nm. The work provides new insights into the surface management of III-V CQDs for high-performance optoelectronic devices.

Supporting Information

The authors have cited additional references within the Supporting Information.[35-47]

Acknowledgements

Conflict of Interest

The authors declare no conflict of interest.

Keywords: indium antimonide • colloidal quantum dots • surface reconstruction • short-wave infrared photodetectors

[1]   M. P. Hansen, D. S. Malchow, *Proc. SPIE* **2008**, *6939*, 69390I.

[2]   F. P. García De Arquer, A. Armin, P. Meredith, E. H. Sargent, *Nat. Rev. Mater.* **2017**, *2*, 16100.

[3]   J. M. Pina, M. Vafaie, D. H. Parmar, O. Atan, P. Xia, Y. Zhang, A. M. Najarian, F. P. Garcia, S. Hoogland, E. H. Sargent, *Nano Lett.* **2022**, *22*, 6802–6807.

[4]   J. Liu, P. Liu, D. Chen, T. Shi, X. Qu, L. Chen, T. Wu, J. Ke, K. Xiong, M. Li, H. Song, W. Wei, J. Cao, J. Zhang, L. Gao, J. Tang, *Nat. Electron.* **2022**, *5*, 443–451.

[5]   Q. Xu, I. T. Cheong, H. Song, V. Van, J. G. C. Veinot, X. Wang, *ACS Photonics* **2022**, *9*, 2792–2801.

[6]   Y. Zhang, M. Vafaie, J. Xu, J. M. Pina, P. Xia, A. M. Najarian, O. Atan, M. Imran, K. Xie, S. Hoogland, E. H. Sargent, *Adv. Mater.* **2022**, *34*, 2206884.

[7]   M. Vafaie, J. Z. Fan, A. Morteza Najarian, O. Ouellette, L. K. Sagar, K. Bertens, B. Sun, F. P. García de Arquer, E. H. Sargent, *Matter* **2021**, *4*, 1042–1053.

WILEY▪VCH

RESEARCH ARTICLE

[8] M. Biondi, M. J. Choi, Z. Wang, M. Wei, S. Lee, H. Choubisa, L. K. Sagar, B. Sun, S. W. Baek, B. Chen, P. Todorović, A. M. Najarian, A. Sedighian Rasouli, D. H. Nam, M. Vafaie, Y. C. Li, K. Bertens, S. Hoogland, O. Voznyy, F. P. García de Arquer, E. H. Sargent, *Adv. Mater.* **2021**, *33*, 2101056.

[9] X. Tang, M. M. Ackerman, M. Chen, P. Guyot-Sionnest, *Nat. Photonics* **2019**, *13*, 277–282.

[10] O. Madelung, U. K. Rößler, M. Schulz, *Group IV Elements, IV-IV and III-V Compounds. Part b-Electronic, Transport, Optical and Other Properties*. Springer, Berlin, **2002**.

[11] F. W. Wise, *Acc. Chem. Res.* **2000**, *33*, 773–780.

[12] C. M. Evans, S. L. Castro, J. J. Worman, R. P. Raffaelle, *Chem. Mater.* **2008**, *20*, 5727–5730.

[13] W. Liu, A. Y. Chang, R. D. Schaller, D. V. Talapin, *J. Am. Chem. Soc.* **2012**, *134*, 20258–20261.

[14] M. Yarema, M. V. Kovalenko, *Chem. Mater.* **2013**, *25*, 1788–1792.

[15] T. Zhao, N. Oh, D. Jishkariani, M. Zhang, H. Wang, N. Li, J. D. Lee, C. Zeng, M. Muduli, H. J. Choi, D. Su, C. B. Murray, C. R. Kagan, *J. Am. Chem. Soc.* **2019**, *141*, 15145–15152.

[16] C. De Mello Donega, S. Busatto, M. De Ruiter, J. T. B. H. Jastrzebski, W. Albrecht, V. Pinchetti, S. Brovelli, S. Bals, M. E. Moret, *ACS Nano* **2020**, *14*, 13146–13160.

[17] D. Zhitomirsky, I. J. Kramer, A. J. Labelle, A. Fischer, R. Debnath, J. Pan, O. M. Bakr, E. H. Sargent, *Nano Lett.* **2012**, *12*, 1007–1012.

[18] M. Liu, O. Voznyy, R. Sabatini, F. P. García De Arquer, R. Munir, A. H. Balawi, X. Lan, F. Fan, G. Walters, A. R. Kirmani, S. Hoogland, F. Laquai, A. Amassian, E. H. Sargent, *Nat. Mater.* **2017**, *16*, 258–263.

[19] B. Sun, A. M. Najarian, L. K. Sagar, M. Biondi, M. J. Choi, X. Li, L. Levina, S. W. Baek, C. Zheng, S. Lee, A. R. Kirmani, R. Sabatini, J. Abed, M. Liu, M. Vafaie, P. Li, L. J. Richter, O. Voznyy, M. Chekini, Z. H. Lu, F. P. García de Arquer, E. H. Sargent, *Adv. Mater.* **2022**, *34*, 2203039.

[20] M.-J. Choi, L. K. Sagar, B. Sun, M. Biondi, S. Lee, A. M. Najjariyan, L. Levina, F. P. García de Arquer, E. H. Sargent, *Nano Lett.* **2021**, *21*, 6057–6063.

[21] M. He, Z. Xu, S.-W. Zhang, M. Zhang, C. Wu, B. Li, J. Li, L. Wang, S. Zhao, F. Kang, G. Wei, *Adv. Photonics Res.* **2022**, *3*, 2100305.

[22] J. Leemans, V. Pejović, E. Georgitzikis, M. Minjauw, A. B. Siddik, Y. H. Deng, Y. Kuang, G. Roelkens, C. Detavernier, I. Lieberman, P. E. Malinowski, D. Cheyns, Z. Hens, *Adv. Sci.* **2022**, *9*, 2200844.

[23] a) C. Kolm, S. A. Kulin, B. L. Averbach, *Phys. Rev.* **1957**, *108*, 965–971. b) A. L. Efros, M. Rosen, *Phys. Rev. B* **1998**, *58*, 7120–7135.

[24] a) A. Y. Chang, W. Liu, D. V Talapin, R. D. Schaller, *ACS Nano* **2014**, *8*, 8513–8519. b) B. Sun, M. Vafaie, L. Levina, M. Wei, Y. Dong, Y. Gao, H. T. Kung, M. Biondi, A. H. Proppe, B. Chen, M. J. Choi, L. K. Sagar, O. Voznyy, S. O. Kelley, F. Laquai, Z. H. Lu, S. Hoogland, F. P. García De Arquer, E. H. Sargent, *Nano Lett.* **2020**, *20*, 3694–3702. c) V. Srivastava, W. Liu, E. M. Janke, V. Kamysbayev, A. S. Filatov, C. J. Sun, B. Lee, T. Rajh, R. D. Schaller, D. V. Talapin, *Nano Lett.* **2017**, *17*, 2094–2101. d) Y. Kim, J. H. Chang, H. Choi, Y. H. Kim, W. K. Bae, S. Jeong, *Chem. Sci.* **2020**, *11*, 913–922.

[25] A. J. Rosenberg, *J. Phys. Chem. Solids* **1960**, *14*, 175–180.

[26] J. Mäkelä, Z. S. Jahanshah Rad, J. P. Lehtiö, M. Kuzmin, M. P. J. Punkkinen, P. Laukkanen, K. Kokko, *Sci. Rep.* **2018**, *8*, 14382.

[27] a) D. Zhu, H. Bahmani Jalali, G. Saleh, F. Di Stasio, M. Prato, N. Polykarpou, A. Othonos, S. Christodoulou, Y. P. Ivanov, G. Divitini, I. Infante, L. De Trizio, L. Manna, *Adv. Mater.* **2023**, *35*, 2303621. b) Y. Zhang, D. Zherebetskyy, N. D. Bronstein, S. Barja, L. Lichtenstein, A. P. Alivisatos, L. W. Wang, M. Salmeron, *ACS Nano* **2015**, *9*, 10445–10452

[28] R. P. Vasquez, B. F. Lewis, F. J. Grunthaner, *J. Appl. Phys.* **1983**, *54*, 1365–1368.

[29] F. L. Lie, A. J. Muscat, *J. Phys. Chem. C* **2011**, *115*, 7440–7449.

[30] M. H. Zarghami, Y. Liu, M. Gibbs, E. Gebremichael, C. Webster, M. Law, *ACS Nano* **2010**, *4*, 2475–2485.

[31] a) Z. Ning, O. Voznyy, J. Pan, S. Hoogland, V. Adinolfi, J. Xu, M. Li, A. R. Kirmani, J. P. Sun, J. Minor, K. W. Kemp, H. Dong, L. Rollny, A. Labelle, G. Carey, B. Sutherland, I. Hill, A. Amassian, H. Liu, J. Tang, O. M. Bakr, E. H. Sargent, *Nat. Mater.* **2014**, *13*, 822–828. b) O. Voznyy, D. Zhitomirsky, P. Stadler, Z. Ning, S. Hoogland, E. H. Sargent, *ACS Nano* **2012**, *6*, 8448–8455.

[32] S. Chatterjee, K. Nemoto, B. Ghosh, H. T. Sun, N. Shirahata, *ACS Appl. Nano Mater.* **2023**, *6*, 15540–15550.

[33] J. Yang, S. Lu, B. Xia, P. Liu, Y. Yang, Z. Xiao, J. Zhang, L. Gao, J. Tang, *Phys. Rev. Appl.* **2023**, *19*, 014021.

[34] a) O. Ouellette, N. Hossain, B. R. Sutherland, A. Kiani, F. P. García De Arquer, H. Tan, M. Chaker, S. Hoogland, E. H. Sargent, *ACS Energy Lett.* **2016**, *1*, 852–857. b) H. Seo, H. J. Eun, A. Y. Lee, H. K. Lee, J. H. Kim, S. W. Kim, *Adv. Sci.* **2023**, 2306439. c) O. Atan, J. M. Pina, D. H. Parmar, P. Xia, Y. Zhang, A. Gulsaran, E. D. Jung, D. Choi, M. Imran, M. Yavuz, S. Hoogland, E. H. Sargent, *Nano Lett.* **2023**, *23*, 4298–4303.

[35] K. Lu, Y. Wang, Z. Liu, L. Han, G. Shi, H. Fang, J. Chen, X. Ye, S. Chen, F. Yang, A. G. Shulga, T. Wu, M. Gu, S. Zhou, J. Fan, M. A. Loi, W. Ma, *Adv. Mater.* **2018**, *30*, 1707572.

[36] J. VandeVondele, M. Krack, F. Mohamed, M. Parrinello, T. Chassaing, J. Hutter, *Comput. Phys. Commun.* **2005**, *167*, 103–128.

[37] J. P. Perdew, K. Burke, M. Ernzerhof, *Phys. Rev. Lett.* **1996**, *77*, 3865–3868.

[38] S. Goedecker, M. Teter, J. Hutter, *Phys. Rev. B* **1996**, *54*, 1703–1710.

[39] J. VandeVondele, J. Hutter, *J. Chem. Phys.* **2007**, *127*, 114105.

[40] P. E. Blöchl, *Phys. Rev. B* **1994**, *50*, 17953–17979.

[41] G. Kresse, J. Furthmüller, *Phys. Rev. B* **1996**, *54*, 11169–11186.

[42] G. Kresse, D. Joubert, *Phys. Rev. B* **1999**, *59*, 1758–1775.

[43] J. P. Perdew, J. A. Chevary, S. H. Vosko, K. A. Jackson, M. R. Pederson, D. J. Singh, C. Fiolhais, *Phys. Rev. B* **1992**, *46*, 6671–6687.

[44] S. Grimme, J. Antony, S. Ehrlich, H. Krieg, *J. Chem. Phys.* **2010**, *132*, 154104.

[45] S. Grimme, S. Ehrlich, L. Goerigk, *J. Comput. Chem.* **2011**, *32*, 1456–1465.

[46] V. M. Le Corre, E. A. Duijnstee, O. El Tambouli, J. M. Ball, H. J. Snaith, J. Lim, L. J. A. Koster, *ACS Energy Lett.* **2021**, *6*, 1087–1094.

[47] S. Lee, M. J. Choi, G. Sharma, M. Biondi, B. Chen, S. W. Baek, A. M. Najarian, M. Vafaie, J. Wicks, L. K. Sagar, S. Hoogland, F. P. G. de Arquer, O. Voznyy, E. H. Sargent, *Nat. Commun.* **2020**, *11*, 4814.

RESEARCH ARTICLE

Entry for the Table of Contents
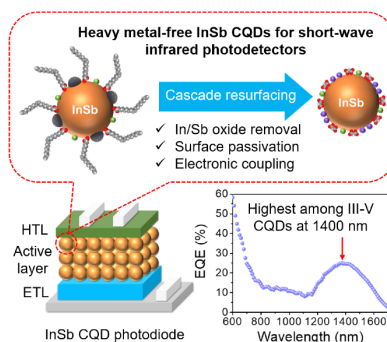
A post-synthetic cascade resurfacing approach is developed for uniform indium antimonide (InSb) colloidal quantum dots (CQDs), which enables removal of native oxides, complete surface passivation, and electronic coupling among CQDs. Short-wave infrared photodetectors fabricated using these resurfaced CQDs as the active layer achieve the highest EQE among III-V CQD photodetectors sensitive to 1400 nm light.